# Role of Si Doping in Reducing Coercive Fields for Ferroelectric Switching in $HfO_2$

Hyemi Yang, Hyun-Jae Lee, Jinhyeong Jo, Chang Hoon Kim, and Jun Hee Lee*
*School of Energy & Chemical Engineering and Department of Energy Engineering, Ulsan National Institute of Science and Technology, 50, UNIST-gil, Ulju-gun, Ulsan 44919, Republic of Korea*

(Received 15 January 2020; revised 31 August 2020; accepted 13 October 2020; published 3 December 2020)

The ferroelectricity of $HfO_2$ thin films is technologically useful with various advantages compared to conventional ferroelectrics. However, the application of orthorhombic $HfO_2$ has been limited by its large coercive field compared to perovskite-based ferroelectrics. Using first-principles calculations, we extensively search for 34 dopant elements to reduce the problematic coercive fields and discover that the coercive fields exhibit a simple volcano shape against the dopant's size. We also discover that the Si dopant is a critical element in stabilizing tetragonal phase $HfO_2$ (transition state) because of its intrinsic $sp^3$ bond favoring characteristics with oxygen, thereby notably lowering the coercive fields. We provide an atomic scale picture to understand the excellent role of Si in effective ferroelectric switching and a simple rule to tune coercive fields with various doping agents.

DOI: 10.1103/PhysRevApplied.14.064012

## I. INTRODUCTION

The recently discovered orthorhombic (*O*) $HfO_2$ has prompted research to develop devices that utilize its robust ferroelectricity at reduced dimensions. $HfO_2$ has attractive advantages compared to conventional perovskite ferroelectrics due to its compatibility with the Si-based CMOS technique and to its scalability to thin films with substantial ferroelectric polarization (approximately 1 nm) [1,2].

However, there are setbacks to devices, such as the large coercive field compared to that of conventional perovskites by one order of magnitude [3]. The large coercive fields used to switch ferroelectric polarization can damage $HfO_2$ films, resulting in electric breakdown and shortening their endurance. A recent research trend focused on reducing the coercive fields using various dopants. Various factors from dopants were studied to tune the coercive fields such as volume change [4,5], monoclinic phase fraction [3], and the dopant size effects [5,6]. Still, the mechanism of why some elements (such as Si) significantly reduce the coercive field has not been fully understood.

We report on how to reduce the coercive field of $HfO_2$ by substitution doping and why Si is a critical element for lowering coercive fields using first-principles simulations. Investigating 34 elements, we find that the energy difference between the tetragonal (*T*) and *O* phase exhibit a volcano shape with respect to the dopant's atomic size. Si is expected to substantially reduce the coercive fields by approximately 50% through stabilization of the tetragonal transition phase. Due to the intrinsic affinity of Si atoms to form $sp^3$ bonds with oxygen, the stabilization of the Si-doped *T* phase is more prevalent than that of the *O* phase. In addition, fast polarization switching is expected through lowering the coercive field. Our theoretical study explains the excellent role of Si in reducing coercive fields and provides a simple method to predict and tune coercive fields using various chemical doping agents.

## II. COMPUTATIONAL METHODS

We conduct first-principles calculations based on density-functional theory (DFT) using Vienna *ab initio* simulation package (VASP) code [7–10]. We adopt a generalized gradient approximation to describe the exchange correlation energy functional and pseudopotentials generated under the projector-augmented plane-wave [11] method by Perdew-Burke-Ernzerhof [12]. The energy cutoff for the plane-wave basis is set to 500 eV, and the force tolerance for the structural optimization is 0.01 eV/Å. For $HfO_2$, a $2 \times 2 \times 2$ *k*-point grid is chosen using the Monkhorst-Pack [13] method for sampling integrations over the Brillouin zone.

The phase transition $E_B$ is calculated using the nudged elastic band method [14] to understand the isosymmetry-promoting structural characteristics induced by doping in a $2 \times 2 \times 2$ supercell containing 96 atoms. All of the figures showing the results of the theoretical calculations are produced using the visualization for electronic and structural analysis (VESTA) code [15].

The exact polarization direction and polarization switching path in $HfO_2$ are not fully uncovered experimentally. While a switching path where oxygen moves across the Hf atomic plane is described in Ref. [5], oxygen also can

*junhee@unist.ac.kr

 

move through the tetragonal transition phase as in Ref. [16]. In addition, various switching paths are reported as in Ref. [17]. This is due to the structural characteristics of $CaF_2$. In contrast to perovskite structures, the $CaF_2$ structure has plural paraelectric centers with respect to the ferroelectric direction (in this paper, the *c* axis). Depending on the different paraelectric centers (Hf layer versus tetragonal), $HfO_2$ can have different polarization directions and switching paths. Among these various paths, we decide on our three switching paths for the following reasons.

(1) According to a recent paper about molecular dynamics (MD) simulations, the tetragonal phase is a transition state during polarization switching [18]. This provides a direct clue to the direction of polarization and switching pathway with respect to the direction of the electric field. (2) The polarization direction is reported as the opposite direction to oxygen displacement based on cubic or tetragonal structures in recent x-ray measurements [19]. (3) As mentioned in Ref. [17], the switching paths through the tetragonal structure are energetically most stable. (4) When a transition from a paraelectric state to a ferroelectric state is observed experimentally, the paraelectric state usually starts at a crystallographic local minimum state. The path through the *Pbcm* transition state, as discussed in Ref. [5], is also one of the possible paths due to the previously mentioned ambiguities. We choose the path through the tetragonal transition state because the *Pbcm* transition state has an unstable structure that has not yet been reported experimentally, which is consistent with the MD results in Ref. [18]. (5) By analyzing the energy differences between each phase (*M*, *O*, and *T* phases) with doping, the effect of the dopant is difficult to see in the *Pbc* because the *Pbcm* transition state is not stabilized or optimized in DFT. (6) Even if there are ambiguities in the polarization directions and switching paths, the fact that the direction of the electric field and oxygen movement are opposite does not change.

To calculate the coercive field in DFT, the most accurate physical quantity determining coercive field is the maximum slope in the curve free energy ($F$) versus Polarization ($P$) while we use the energy difference ($\Delta E$) between high and low symmetric structure [in this case, transition ($T$) phase and ferroelectric ($O$) phase]. Of course, in real ferroelectrics, the polarization switching proceeds via a combination of domain-wall nucleation and growth (propagation). Therefore, coercive field does not correspond directly to the energy landscape nor energy difference from first-principles calculations. However, the energy difference has proven to be a kind of useful indicator in estimating switching energy barrier and coercive field, because the energy barrier increases as the energy difference between high and low symmetric structures increases. Previous studies have already employed $\Delta E$ as an indicator of estimating the height of the energy barrier and *Ec* [20–29]. So, we expect that the energy difference between the two phases and coercive field will have a similar tendency.

## III. RESULTS AND DISCUSSION

In this section, we show the results of simulation using the VASP code for doping's effect on pristine $HfO_2$. To date, among various dopants, Si has attracted considerable attention because of its stable ferroelectric *O*-phase structure in films and its role in lowering coercive fields [30]. Based on a study by Park *et al*., we choose 34 species for simulations to discover dopants with superior ability compared to Si taking into account the oxygen-rich conditions [31]. All of the dopants are substituted for Hf atom(s) in supercells consisting of 96 atoms ($2 \times 2 \times 2$) to prepare concentrations of 3.125% and 6.25%, respectively. We present dopant candidates that stabilize the *O* phase relative to the ground-state monoclinic ($M$) phase and induce low coercive fields.

### A. Relationship to the ionic radius

We calculate the energy difference between the $M$ and $T$ and/or $O$ phases of $HfO_2$ in the presence of dopants. Figure 1 shows the relative energies of the $O$ phase (green) and $T$ phase (orange) with respect to the $M$ phase (ground state) at (a) 3.125% and at (b) 6.25% doping concentrations. The relative energies induced by various dopants are plotted against their ionic radius to check the structural stabilities. In both the *O*- and *T*-phase structures, a larger difference in dopant size compared to the size of the Hf atom results in a smaller energy difference from the $M$ phase and thus strengthens structural stabilities of both the $O$ and $T$ phases against the $M$ phase. Among the dopants studied, Si shows the highest stability in the $T$ phase and Ba in the $O$ phase; the volcano plot tends to be more prominent at a doping concentration of 6.25% [Fig. 1(b)] than 3.125% [Fig. 1(a)]. The value of $\Delta E(T) = E(T) - E(M)$ in pristine cases is 162.58 meV f.u.$^{-1}$ and $\Delta E(O) = E(O) - E(M)$ is 84.30 meV f.u.$^{-1}$. With Si doping, $\Delta E(T)$ is reduced to 113.84 meV f.u.$^{-1}$ at a 3.125% doping concentration and to 85.52 meV f.u.$^{-1}$ at 6.25%, clearly demonstrating *T*-phase stabilization by Si. In contrast, $\Delta E(O)$ is reduced to 77.53 meV f.u.$^{-1}$ at a 3.125% doping concentration and 61.35 meV f.u.$^{-1}$ at 6.25%. These results are in good agreement with a previous study demonstrating that Si doping imposes a significant effect on the stabilization of *T* phase $HfO_2$ [35].

According to a study by Maeda *et al*. describing the switching pathways of $HfO_2$, the energy difference between the $T$ and $O$ phases is related to the coercive fields in polarization switching [17]. We also infer that the coercive field and $E(T - O)$=$E(T$, paraelectric$) - E(O$, ferroelectric$)$ are interrelated with each other. $E(T - O)$ calculated from first principles and the experimentally observed coercive field are plotted against the ionic radius

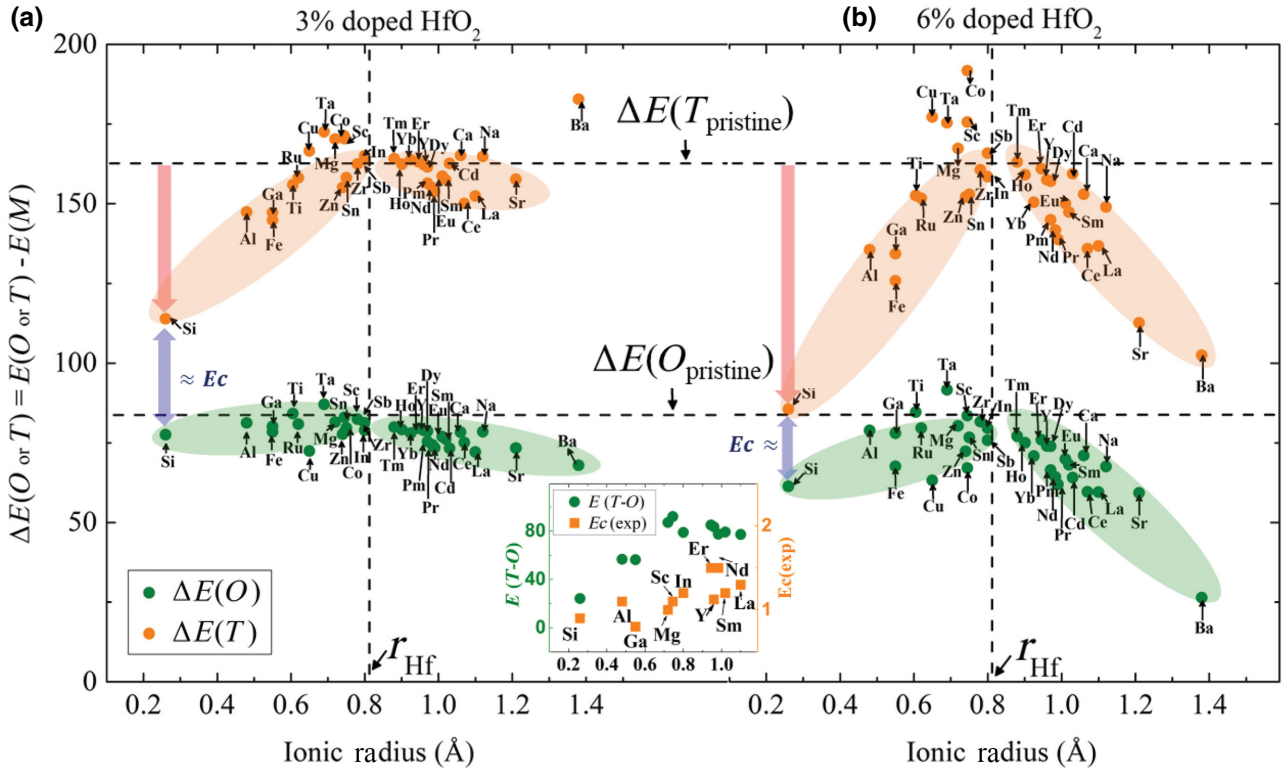


FIG. 1. Energy differences of $O$ ($Pca2_1$) and $T$ phase ($P4_2/nmc$) to the $M$ phase ($P2_1/c$) for each dopant with (a) 3.125% (in short 3%) and (b) 6.25% (in short 6%) doping concentration plotted versus the ionic radius. (Inset) Relationship between the simulated $E(T-O)$ and experimental coercive field as a function of the ionic radius. (Si, Y, Al, La, Ref. [30]; Ga, In, Mg, Ref. [32]; Sc, Ref. [3]; Sm, Nd, Er, Ref.[33,34]).

in the inset of Fig. 1. In the inset, we can observe a roughly linearlike relationship between these two factors. Actually, the correlation between $E(T-O)$ and experimental coercive field is not exactly linear because our DFT results do not include external factors that could be incorporated in the real experimental conditions such as oxygen vacancies, local strain and grain boundaries. These external factors could affect to the $T$-phase stability and coercive field. For example, low charged dopants like Ga(+3) and Mg(+2) than Hf(+4) could induce oxygen vacancies, which were reported to reduce the coercive field [36,37] and $E(T-O)$ [38]. Even though these additional vacancies contribute to reducing the coercive field, we did not treat the oxygen vacancies in this paper. When we assume an ideal condition where no oxygen vacancy is present, the ability to lower the coercive field is expected to be significantly large for Si among the various dopant candidates because the structural stabilization of the $T$ phase by Si is quite remarkable.

### B. Phonon-mode analysis

To learn more about the microscopic factors that lead to the significant $T$-phase stabilization by Si, the structures of the doped $O$ and $T$ phases are decomposed into relevant phonon modes [39] [Eqs. (S1)–(S2), and Fig. S1 within the Supplemental Material [40]]. Among the various dopants, for comparison with Si (smaller than Hf), La dopant is chosen as a larger representative element since a number of previous experiments presented its prominent structural stabilization [6,30,33,41]. We discover that Si doping causes significant structural deformation that enhances the structural stability of the $T$ phase in contrast to La doping.

Figure 2 shows the phonon-mode analysis of $T$- and $O$-phase structures doped with (a) Si and (b) La at 0%, 3.125%, and 6.25% concentrations, respectively. In the Si, changes in all of the phonon-mode displacements in both the $T$ and $O$ phases are prominent. In particular, the $X_2^{'}$ mode, which is the unique mode in the $T$ phase, increases in proportion to the Si doping concentration. However, in the La, both the $T$ and $O$ phases show negligibly small changes in the phonon-mode displacements. In particular, in the $T$ phase, the $X_2^{'}$ mode tends to slightly decrease with the La doping ratio (for changes in the phonon-mode displacement, see Fig. S2 within the Supplemental Material [40]). Since the $X_2^{'}$ mode stabilizes the $T$ phase, the results are related to the superior structural stability of the Si-doped $T$ phase to the stability of the La-doped $T$ phase as shown in Fig. 1.

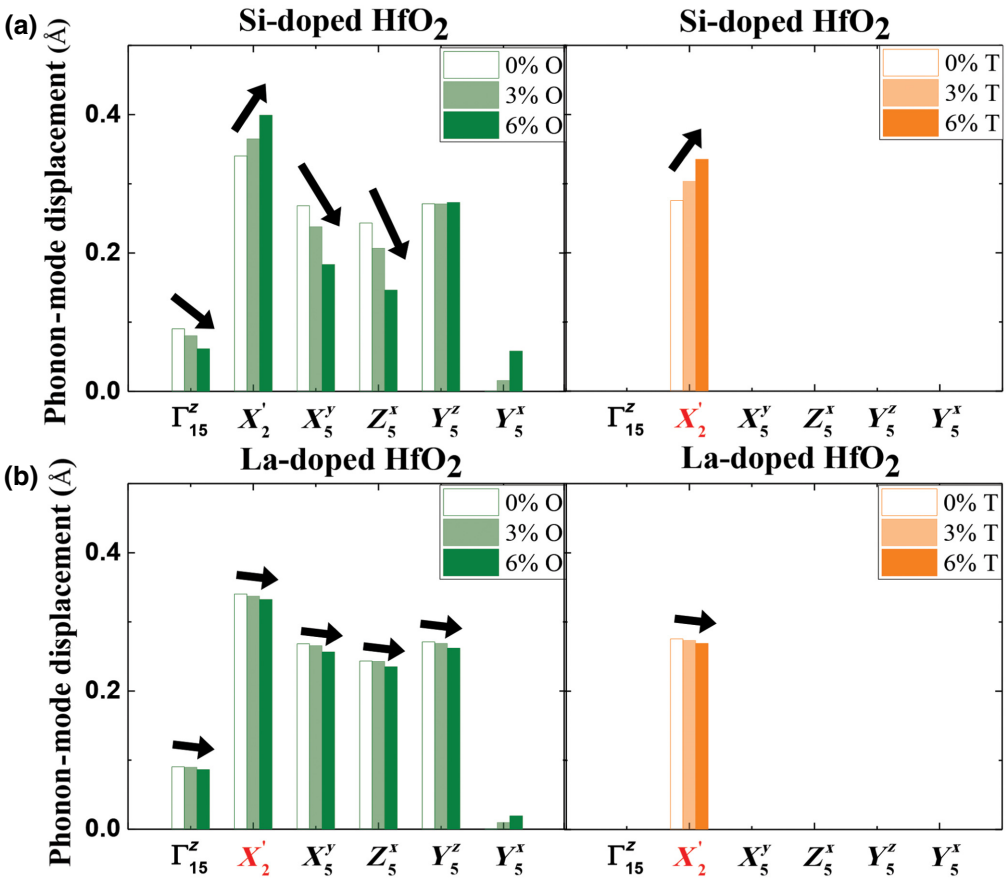


FIG. 2. Phonon-mode displacement of (a) Si-doped and (b) La-doped $O$ ($Pca2_1$, left) and $T$ ($P4_2/nmc$, right) phases for pristine (0%), 3.125% (in short 3%), and 6.25% (in short 6%) doping concentrations.

In the pristine $T$-phase $HfO_2$, there is only one $X_2'$ mode among the six modes. Thus, the structural distortion of the $T$ phase by the dopant should appear only through a change in the $X_2'$ mode displacement. In other words, the improved structural stability of the $T$ phase structure seems to be directly related to the increase in $X_2'$ mode displacement as a result of doping. In the case of Si doping, the $X_2'$ mode displacement dramatically increases, while with La, the $X_2'$ mode displacement slightly decreases. This observation implies that Si doping increases the $T$-phase components, resulting in the relevant $T$-phase stabilization.

### C. Structural analysis

Based on the phonon-mode analysis, we conduct additional structural analysis and find that Si forms a more condensed $sp^3$ bonding network with nearest oxygen atoms in the $T$-phase $HfO_2$ structure. Figure 3 shows the results of a structural analysis of relaxed tetragonal Si- and La-doped $HfO_2$. In contrast to La doping [Fig. 3(a)], the local oxygen structure around the Si-doping site [Fig. 3(b)] has a tetragonal structure driven by the $sp^3$ bonding network.

Moreover, as shown in Fig. 3(c), the Hf atom in the pristine $T$-phase $HfO_2$ has four bonds with the nearest oxygen atoms. While Si has four bonds as demonstrated in Fig. 3(b), La has eight bonds with the nearest oxygen atoms as shown in Fig. 3(a). As indicated in Fig. 3(c), when the oxygen atoms move along the $X_2'$ mode direction (black arrows), the original eight bonds with oxygen in the original cubic ($C$) phase are reduced to four bonds. Therefore, only the four oxygen atoms shown in pink participate in the bond with the central Hf atom by the $X_2'$ mode and eventually strengthen the tetrahedral $sp^3$ bond characteristics. When Si is doped into the pristine $T$-phase structure, the original $sp^3$ bond environment due to the $X_2'$ mode in the $T$-phase actively reacts with the Si dopant and forms a local $SiO_2$ (quartz) structure to further stabilize the $T$-phase structure. In other words, the local $SiO_2$ (quartz) structure creates a more condensed tetrahedral structure, increasing the $X_2'$ mode displacement and eventually enhancing the $T$-phase structural stability.

In the La, unlike the pristine $T$-phase structure, there are eight La bonds with the nearest oxygen atoms showing a tendency toward the $C$ phase rather than the $T$ phase [Fig. 3(a)]. This change in the oxygen environment is expected to reduce the $T$-phase component, with smaller $X_2'$ mode displacement and less ability to induce structural stability. Therefore, we suggest that the Si dopant is a special case that causes structural deformation with a $sp^3$ bond and subsequently decreases the coercive fields.

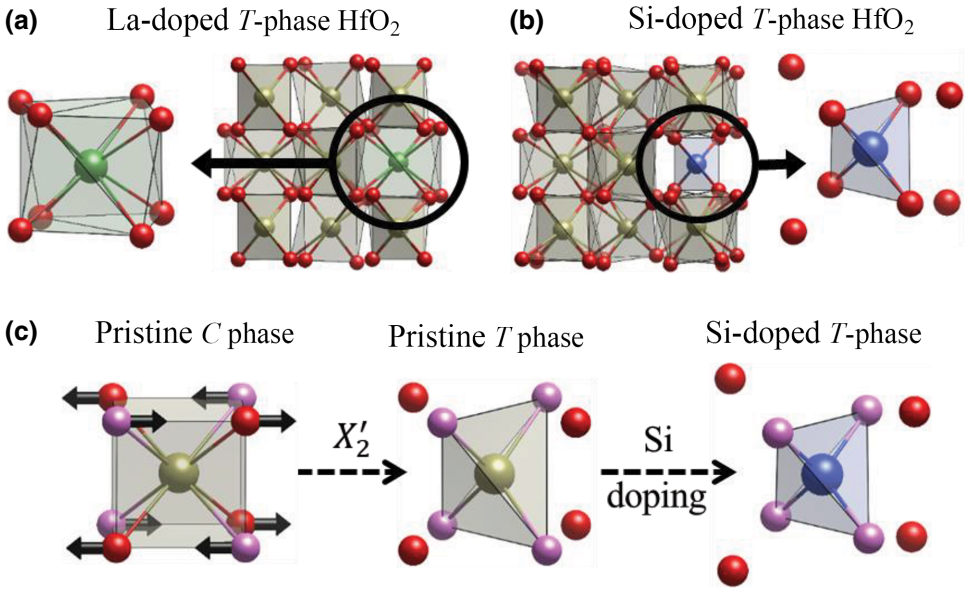


FIG. 3. The structural difference between (a) La (green spheres) and (b) Si (blue spheres)-doped $T$-phase ($P4_2/nmc$) structures. (c) Structural deformation induced by condensation of the $X_2'$ mode (denoted by the black arrows) and Si doping. The pink spheres indicate that an oxygen atom is involved in the $sp^3$ bond with the central atom.

### D. Phase transition of polarization switching

Motivated by the observation that the coercive field is roughly proportional to the simulated $E(T-O)$, we hypothesize that the significant $T$-phase stabilizer, Si, will reduce the coercive fields to enable faster and more efficient ferroelectric switching. Figure 4 shows the results of polarization switching using nudged elastic band (NEB) calculations from the $O$ phase (down, $\lambda = -1$) to the $O$ phase (up, $\lambda = 1$) with (a) pristine, (b) Si, and (c) La doping. As shown in Fig. 4(a), the switching calculation is conducted with respect to three pathways to understand the effects of the coercive fields. If in these three paths, the

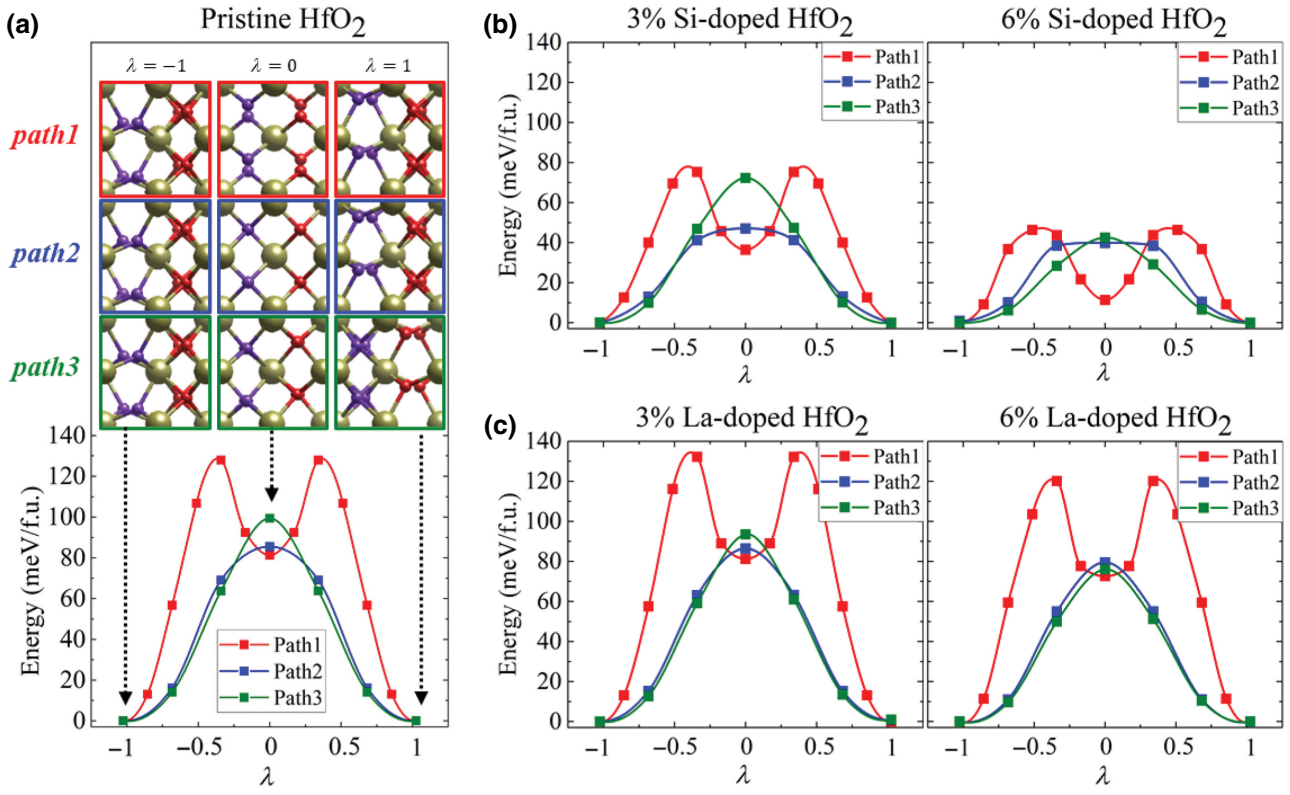


FIG. 4. Three ferroelectric switching pathways of (a) pristine, (b) Si-, and (c) La-doped cases at 3.125% (in short 3%) and 6.25% (in short 6%) doping concentrations. λ denotes the polar displacement, $\lambda = -1$ (FE, negative), $\lambda = 0$ (PE, zero), and $\lambda = 1$ (FE, positive).

structure goes through the tetragonal phase, there should be an energy local minimum in the energy profile (path 1), since the tetragonal phase is metastable, rather than unstable with respect to switching paths.

However, the most favorable switching routes from the $O$ phase (polarization down, $\lambda = -1$) to the $O$ phase (polarization up, $\lambda = 1$) are paths 2 and 3. Path 2 is a route where only the $X_2^{'}$ mode survives in the transition state ($\lambda = 0$, tetragonal), exhibiting only an active left oxygen layer (purple) moving from the down to the up position for switching. Path 3 is a route where both $X_2^{'}$ and $Y_5^{z}$ modes simultaneously survive in the transition state (tetragonal $X_2^{'}$ with the inclusion of the $Y_5^{z}$ mode), exhibiting that all of the oxygen is displaced during the switching. Path 1 is a switching route in which the direction of the $X_2^{'}$ mode, which is the x axis in the o-phase, is rotated to the z axis in the transition state (tetragonal with a rotated $X_2^{'}$ mode direction to the $z$ axis), necessitating activation energy during the $X_2^{'}$ mode rotation from the $x$ to $z$ axis, resulting in a triple-well switching energy shape (Fig. S3−S4 within the Supplemental Material [40]).

For pristine $HfO_2$, the switching energy barrier ($E_B$) is 80–130 meV f.u.$^{-1}$ [Fig. 4(a)]. When Si is used as a dopant, $E_B$ significantly decreases to 40–80 meV f.u.$^{-1}$ (3.125%) and eventually to 15–45 meV f.u.$^{-1}$ (6.25%) with an increase in the doping concentration. However, for La, $E_B$ remains high at approximately 80–130 meV f.u.$^{-1}$, and La doping is not expected to reduce the coercive fields. As the doping concentration increases, $E_B$ decreases considerably because of the stabilization of the $T$ phase by Si doping but not in the case of La doping. These results are consistent with those demonstrated in Fig. 1, which shows that $E(T - O)$ is proportional to the coercive field.

## IV. CONCLUSION

Hafnia is a promising ferroelectric that can potentially be integrated into silicon devices; however, due to its higher magnitude coercive fields compared to other ferroelectrics, it is difficult to reduce the switching power. To understand the atomic level mechanisms of tuning coercive fields, we analyze the effects of 34 dopants on the structural stabilities of the transition and ferroelectric states. We show that $E(T - O)$ (the energy difference between the transition and ferroelectric states) exhibit a simple volcano shape against the dopant's size so that we can roughly estimate the corresponding coercive field with respect to the dopant's size. Furthermore, phonon-mode analysis is conducted to determine why Si is an excellent element at reducing coercive fields. We find that the $X_2^{'}$ mode displacement of the transition $T$-phase structure increased significantly when it was doped with Si because the Si dopant strongly reacted with the $sp^3$ oxygen environment in the pristine $T$ phase. Hence, the Si dopant locally formed a quartz structure, which further increased the stability of the structures by doping. The unique $T$ phase (transition state) stabilizing characteristics of Si reduced the polarization switching barrier from the $O$ phase (up) to the $O$ phase (down) through the $T$ phase. Furthermore, the parent phase of the functional ferroelectric orthorhombic ($Pca2_1$) phase is the tetragonal phase [42–45]. In other words, $HfO_2$ adopts the tetragonal (or cubic) phase at a high temperature and then transforms to the $Pca2_1$ phase after being annealed or applied with an electric field with a proper thickness and/or a doping concentration while the ground state of $HfO_2$ is still a monoclinic phase. Thus, to stabilize the ferroelectric phase, not only the energy difference between tetragonal and orthorhombic phases [$E(T - O)$] but also the energy difference between orthorhombic and monoclinic phases [$E(O - M)$] need to be reduced. In the experimental point of view, we also suggest that Si doping provides a proper condition to stabilize the ferroelectric phase ($Pca2_1$) by reducing both $E(T - O)$ and $E(O - M)$, simultaneously.

There is still little research on how the individual dopant characteristics affect the ferroelectric switching. Thus, this study provides microscopic illustrations on how the individual chemical properties of the doping elements influence ferroelectric switching pathways, which can be used as a tool to understand experiments on the doping effects on the coercive field in the future.

## ACKNOWLEDGMENTS

Financial support from the Creative Materials Discovery (Grant No. 2017M3D1A1040828), the MOTIE (Ministry of Trade, Industry Energy) (Grant No. 10080657), KRSC (Korea Semiconductor Research Consortium) program, Mid-career Researcher Program (Grant No. 2020R1A2C2103126) and the Research Project Funded by U-K Brand (Grants No. 1.200033.01 and No. 1.200030.01). We also appreciate the supercomputing resources, including technical support, supplied by the Supercomputing Center/Korea Institute of Science and Technology Information (Grant No. KSC-2020-CRE-0088).

[1] M. H. Park, Y. H. Lee, T. Mikolajick, U. Schroeder, and C. S. Hwang, Review and perspective on ferroelectric $HfO_2$-based thin films for memory applications, MRS Communications **8**, 795 (2018).

[2] H.-J. Lee *et al.*, Scale-free ferroelectricity induced by flat phonon bands in $HfO_2$, Science **369**, 1343 (2020).

[3] L. Xu, S. Shibayama, K. Izukashi, T. Nishimura, T. Yajima, S. Migita, and A. Toriumi, in *2016 IEEE International Electron Devices Meeting (IEDM)* (IEEE, 2016), pp. 25.2.1.

[4] C. Künneth, R. Materlik, M. Falkowski, and A. Kersch, Impact of four-valent doping on the crystallographic phase formation for ferroelectric $HfO_2$ from first-principles: Implications for ferroelectric memory and energy-related applications, ACS Appl. Nano Mater. **1**, 254 (2017).

[5] S. Clima, D. Wouters, C. Adelmann, T. Schenk, U. Schroeder, M. Jurczak, and G. Pourtois, Identification of the ferroelectric switching process and dopant-dependent switching properties in orthorhombic $HfO_2$: A first principles insight, Appl. Phys. Lett. **104**, 092906 (2014).

[6] U. Schroeder, E. Yurchuk, J. Müller, D. Martin, T. Schenk, P. Polakowski, C. Adelmann, M. I. Popovici, S. V. Kalinin, and T. Mikolajick, Impact of different dopants on the switching properties of ferroelectric hafniumoxide, Jpn. J. Appl. Phys. **53**, 08LE02 (2014).

[7] G. Kresse and J. Furthmüller, Efficiency of ab-initio total energy calculations for metals and semiconductors using a plane-wave basis set, Comput. Mater. Sci. **6**, 15 (1996).

[8] G. Kresse and J. Furthmüller, Efficient iterative schemes for ab initio total-energy calculations using a plane-wave basis set, Phys. Rev. B **54**, 11169 (1996).

[9] G. Kresse and J. Hafner, Ab initio molecular dynamics for liquid metals, Phys. Rev. B **47**, 558 (1993).

[10] G. Kresse and D. Joubert, From ultrasoft pseudopotentials to the projector augmented-wave method, Phys. Rev. B **59**, 1758 (1999).

[11] P. E. Blöchl, Projector augmented-wave method, Phys. Rev. B **50**, 17953 (1994).

[12] J. P. Perdew, K. Burke, and M. Ernzerhof, Generalized gradient approximation made simple, Phys. Rev. Lett. **77**, 3865 (1996).

[13] H. J. Monkhorst and J. D. Pack, Special points for Brillouin-zone integrations, Phys. Rev. B **13**, 5188 (1976).

[14] D. Sheppard, P. Xiao, W. Chemelewski, D. D. Johnson, and G. Henkelman, A generalized solid-state nudged elastic band method, J. Chem. Phys. **136**, 074103 (2012).

[15] K. Momma and F. Izumi, VESTA 3 for three-dimensional visualization of crystal, volumetric and morphology data, J. Appl. Crystallogr. **44**, 1272 (2011).

[16] T. D. Huan, V. Sharma, G. A. Rossetti Jr, and R. Ramprasad, Pathways towards ferroelectricity in hafnia, Phys. Rev. B **90**, 064111 (2014).

[17] T. Maeda, B. Magyari-Kope, and Y. Nishi, in *2017 IEEE International Memory Workshop (IMW)* (IEEE, 2017), pp. 1.

[18] P. Fan, Y. Zhang, Q. Yang, J. Jiang, L. Jiang, M. Liao, and Y. Zhou, Origin of the intrinsic ferroelectricity of $HfO_2$ from ab initio molecular dynamics, J. Phys. Chem. C **123**, 21743 (2019).

[19] S. S. Cheema, D. Kwon, N. Shanker, R. Dos Reis, S.-L. Hsu, J. Xiao, H. Zhang, R. Wagner, A. Datar, and M. R. McCarter, Enhanced ferroelectricity in ultrathin films grown directly on silicon, Nature **580**, 478 (2020).

[20] R. Xu, R. Gao, S. E. Reyes-Lillo, S. Saremi, Y. Dong, H. Lu, Z. Chen, X. Lu, Y. Qi, and S.-L. Hsu, Reducing coercive-field scaling in ferroelectric thin films via orientation control, ACS Nano **12**, 4736 (2018).

[21] S. Song, H. M. Jang, N.-S. Lee, J. Y. Son, R. Gupta, A. Garg, J. Ratanapreechachai, and J. F. Scott, Ferroelectric polarization switching with a remarkably high activation energy in orthorhombic $GaFeO_3$ thin films, NPG Asia Mater. **8**, e242 (2016).

[22] K. F. Garrity, High-throughput first-principles search for new ferroelectrics, Phys. Rev. B **97**, 024115 (2018).

[23] S. Beckman, X. Wang, K. M. Rabe, and D. Vanderbilt, Ideal barriers to polarization reversal and domain-wall motion in strained ferroelectric thin films, Phys. Rev. B **79**, 144124 (2009).

[24] J. W. Bennett, K. F. Garrity, K. M. Rabe, and D. Vanderbilt, Hexagonal A B C semiconductors as ferroelectrics, Phys. Rev. Lett. **109**, 167602 (2012).

[25] J. W. Bennett, K. F. Garrity, K. M. Rabe, and D. Vanderbilt, Orthorhombic A B C semiconductors as antiferroelectrics, Phys. Rev. Lett. **110**, 017603 (2013).

[26] N. A. Benedek and C. J. Fennie, Hybrid improper ferroelectricity: A mechanism for controllable polarization-magnetization coupling, Phys. Rev. Lett. **106**, 107204 (2011).

[27] J. W. Bennett and K. M. Rabe, Integration of first-principles methods and crystallographic database searches for new ferroelectrics: Strategies and explorations, J. Solid State Chem. **195**, 21 (2012).

[28] R. E. Cohen, Origin of ferroelectricity in perovskite oxides, Nature **358**, 136 (1992).

[29] K. Rabe, in *Functional Metal Oxides: New Science and Novel Applications*, edited by SB Ogale, TV Venkatesan & MG Blamire, ch. 7 (John Wiley and Sons, New York, 2013).

[30] M. H. Park, Y. H. Lee, H. J. Kim, Y. J. Kim, T. Moon, K. D. Kim, J. Mueller, A. Kersch, U. Schroeder, and T. Mikolajick, Ferroelectricity and antiferroelectricity of doped thin $HfO_2$-based films, Adv. Mater. **27**, 1811 (2015).

[31] R. Materlik, C. Künneth, T. Mikolajick, and A. Kersch, The impact of charge compensated and uncompensated strontium defects on the stabilization of the ferroelectric phase in $HfO_2$, Appl. Phys. Lett. **111**, 082902 (2017).

[32] S. Starschich and U. Boettger, An extensive study of the influence of dopants on the ferroelectric properties of $HfO_2$, J. Mater. Chem. C **5**, 333 (2017).

[33] S. Starschich, D. Griesche, T. Schneller, and U. Böttger, Chemical solution deposition of ferroelectric hafnium oxide for future lead free ferroelectric devices, ECS J. Solid State Sci. Technol. **4**, P419 (2015).

[34] J. D. Anderson, J. Merkel, D. Macmahon, and S. K. Kurinec, Evaluation of Si: $HfO_2$ ferroelectric properties in MFM and MFIS structures, IEEE J. Electron. Devices Society **6**, 525 (2018).

[35] C.-K. Lee, E. Cho, H.-S. Lee, C. S. Hwang, and S. Han, First-principles study on doping and phase stability of $HfO_2$, Phys. Rev. B **78**, 012102 (2008).

[36] S. Clima, S. McMitchell, K. Florent, L. Nyns, M. Popovici, N. Ronchi, L. Di Piazza, J. Van Houdt, and G. Pourtois, in *2018 IEEE International Electron Devices Meeting (IEDM)* (IEEE, 2018), pp. 16.5. 1.

[37] Y. Zhou, Y. Zhang, Q. Yang, J. Jiang, P. Fan, M. Liao, and Y. Zhou, The effects of oxygen vacancies on ferroelectric phase transition of $HfO_2$-based thin film from first-principle, Comput. Mater. Sci. **167**, 143 (2019).

[38] M. Falkowski, C. Künneth, R. Materlik, and A. Kersch, Unexpectedly large energy variations from dopant

interactions in ferroelectric $HfO_2$ from high-throughput ab initio calculations, npj Comput. Mater. **4**, 1 (2018).

[39] S. E. Reyes-Lillo, K. F. Garrity, and K. M. Rabe, Antiferroelectricity in thin-film $ZrO_2$ from first principles, Phys. Rev. B **90**, 140103 (2014).

[40] See Supplemental Material at http://link.aps.org/supplemental/10.1103/PhysRevApplied.14.064012 for details of the method for phonon-mode analysis and amplitude of phonon modes.

[41] U. Schroeder, C. Richter, M. H. Park, T. Schenk, M. Pesic, M. Hoffmann, F. P. Fengler, D. Pohl, B. Rellinghaus, and C. Zhou, Lanthanum-doped hafnium oxide: A robust ferroelectric material, Inorg. Chem. **57**, 2752 (2018).

[42] T. Böscke, J. Müller, D. Bräuhaus, U. Schröder, and U. Böttger, Ferroelectricity in hafnium oxide thin films, Appl. Phys. Lett. **99**, 102903 (2011).

[43] M. Pešić, F. P. G. Fengler, L. Larcher, A. Padovani, T. Schenk, E. D. Grimley, X. Sang, J. M. LeBeau, S. Slesazeck, and U. Schroeder, Physical mechanisms behind the field-cycling behavior of $HfO_2$-based ferroelectric capacitors, Adv. Funct. Mater. **26**, 4601 (2016).

[44] M. H. Park, H. J. Kim, Y. J. Kim, Y. H. Lee, T. Moon, K. D. Kim, S. D. Hyun, and C. S. Hwang, Study on the size effect in $Hf_{0.5}Zr_{0.5}O_2$ films thinner than 8nm before and after wake-up field cycling, Appl. Phys. Lett. **107**, 192907 (2015).

[45] M. Hoffmann, U. Schroeder, C. Künneth, A. Kersch, S. Starschich, U. Böttger, and T. Mikolajick, Ferroelectric phase transitions in nanoscale $HfO_2$ films enable giant pyroelectric energy conversion and highly efficient supercapacitors, Nano Energy **18**, 154 (2015).